Overview

In the supplementary material, additional details that are not included in the main paper due to space limits are provided as follows:

- Explanation on the chosen frequency ratio between ν_1 and ν_2 (see Section 1).
- Accuracy results for other random interferometric configurations (see Section 2).
- Details on the bandwidth limits for full sky spectral coherence
- Justification for the impact of the instrumental errors
- Details on the Pipeline setup and internal methods

1 Choice of the factor between ν_1 and ν_2

The Radio-Source Tracker (RST) algorithm requires measuring the direction of the main radio source in the sky. This is done using interferometric observations performed at a chosen frequency ν_2. This frequency is chosen to ensure a given spatial resolution for the interferometer. In the context of the *Lost-In-Space* mode of the Radio-Source Tracker, the instrument has no prior knowledge of the location of the target sources and has to scan the entire sky. Here, we propose to perform this coarse localization by computing a low-resolution image of the entire sky of size $\Omega_1 = 4\pi$ sr from observations at an intermediate lower frequency, ν_1. For an interferometer of size $D_{\max}$, the spatial resolution at this frequency is $\theta_{\text{res},1} = c/(D_{\max}\nu_1)$. By using a discretization of the full sky in pixels of equal area (with HEALPix Gorski et al. (2005), the total number of pixels required to image the entire sky is:

$$N_{\text{pix},1} = \frac{\Omega_1}{{\theta_{\text{res}1}}^2} = 4\pi\Big(\frac{D_{\max}}{c}\Big)^2\nu_1^2 \tag{1}$$

The second image produced by the RST is centered on the brightest pixel of the first image and covers an area of radius $\sqrt{\Omega_2} = 5\theta_{\text{res},1}$, which is 5 times the theoretical spatial resolution at the frequency ν_1. This factor of 5 is a margin to ensure that the source is not missed in the second image. An increased spatial resolution of $\theta_{\text{res},2} = c/(D\nu_2)$ requires a higher observational frequency $\nu_2 > \nu_1$. Therefore, the number of pixels in the zoomed region is:

$$N_{\text{pix},2} = \left(\frac{\sqrt{\Omega_2}}{\theta_{\text{res},2}}\right)^2 = (5\nu_2/\nu_1)^2 \tag{2}$$

The total number of pixel values to compute in order to produce these two images is given by:

$$\begin{aligned} N_{\text{pix, tot}} &= 4\pi\Big(\frac{D_{\max}}{c}\Big)^2\nu_1^2 + 5^2\Big(\frac{\nu_2}{\nu_1}\Big)^2 \\ &= 4\pi\Big(\frac{D_{\max}}{c}\Big)^2\Big(\frac{\nu_2}{\gamma}\Big)^2 + 5^2\gamma^2 \end{aligned} \tag{3}$$

where $\gamma = \nu_2/\nu_1$ is the ratio between the two frequencies.

For a given spatial resolution of the RST, ν_2 is fixed and the value of γ that minimizes the number of computed pixels is given by:

$$\begin{aligned}
&\frac{\partial N_{\text{pix, tot}}}{\partial \gamma}\Big|_{\gamma_{\text{opt}}} = 0 \\
\iff\ & -8\pi\Big(\frac{D_{\max}}{c}\Big)^2 \nu_2^2 \frac{1}{\gamma_{\text{opt}}^3} + 50\gamma_{\text{opt}} = 0 \\
\iff\ & \gamma_{\text{opt}}^4 = 8\pi\Big(\frac{D_{\max}}{c}\Big)^2 \nu_2^2 \frac{1}{50} \\
\iff\ & \gamma_{\text{opt}} = (4\pi)^{1/4}\sqrt{\frac{D_{\max}\nu_2}{5c}}
\end{aligned} \tag{4}$$

For $D_{\max} = 100$ km and $\nu_2 = 300$ kHz, the optimal ratio is $\gamma_{\text{opt}} = 8.4$. This optimum depends on the observation frequency ν_2. With $\nu_2 = 5$ MHz, the optimal ratio is $\gamma_{\text{opt}} = 34.4$.

As HEALPix maps' resolutions are given by powers of 2, the choice of $\gamma = 2^3$ seems to be well suited to minimize the computation costfor our simulated frequencies while taking advantage of HEALPix discretization.

2 RST's accuracy for other interferometric configurations

The RST's accuracy results presented in Figure 4 in the main article are given for a unique swarm configuration. The same graphic is provided for 2 other random configurations in Figure S1. A similar behavior can be observed for each configuration for a high level of noise $1/\sqrt{2\Delta\nu\tau} > 10^{-2}$ (right side). However, at lower noise levels, the RST's accuracy trends are less similar. It shows that in this regime, the accuracy is mostly dictated by the interferometric configuration rather than the noise.

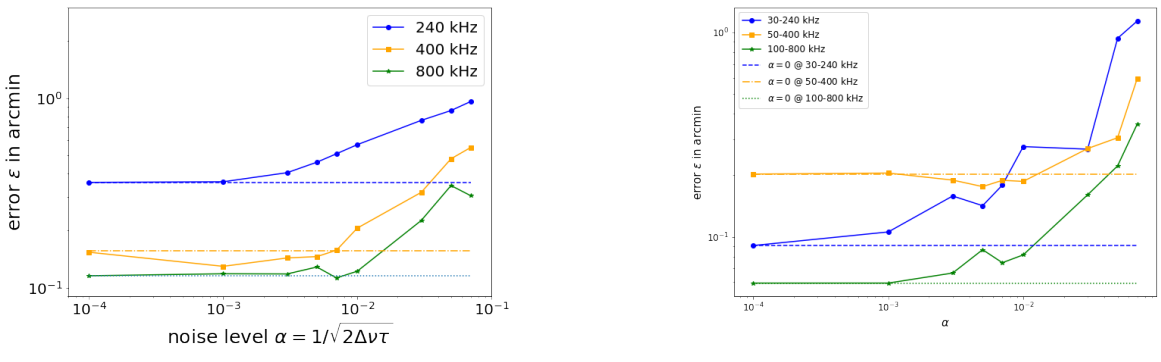

(a) (b)

Figure S1: RST's accuracy as a function of noise for two different random swarm configurations shown in panels (a) and (b).

3 Full sky spectral coherence

The RST's Lost-In-Space mode requires producing snapshot images of the full sky in order to detect sources from any direction. Therefore, the data acquired to produce those images have to be coherent for all directions of the sky. Spectral integration may cause a loss of coherence if chosen too wide. The spectral bandwidth has to be selected small enough to ensure full sky spectral coherence.

For a given baseline vector $\vec{b}$ performing observations with a bandwidth of $\Delta\nu$, the spectral coherence of a source in direction $\vec{s}$ is expressed as (Thompson et al., 2017):

$$C^{b}_{\Delta\nu}(\vec{s}) = \mathrm{sinc}(\pi \frac{\Delta\nu}{c} \vec{b} \cdot \vec{s}) \tag{5}$$

where c is the speed of light.

This expression is the spectral coherence map over the whole sky for any direction $\vec{s}$. If this term is equal to 1 for any direction, this means that the observation is coherent for the full sky.

This is verified for a baseline when $\Delta\nu \ll c/|\vec{b}|$, which is when the bandwidth is negligible compared to the inverse of the coherence duration ($D_{\max}/c$). This is verified for every baseline of the interferometer with a bandwidth such as $\Delta\nu \ll c/D_{\max}$ with $D_{\max}$ being the longest length of the baselines. In the case of NOIRE, a full sky coherence with $C_{\Delta\nu} > 0.9$ is achieved with a bandwidth of 0.5 kHz. With this bandwidth, the spectral decoherence does not reduce the gain by more than 10 % for any direction in the sky.

4 Impact of the instrumental errors

The errors in the instrument parameters affect the phase of the visibilities. let us denote Δb as the baseline error, and δT as the clock offset for a given baseline. The phase bias induced by those errors is given by:

$$\phi_{\mathrm{err}} = k(c\Delta T + \Delta b) \tag{6}$$

Let $dl = c\Delta T + \Delta b$ be the length error.

This translates to a maximal pointing error of:

$$\theta_{\mathrm{err}} = \frac{\phi_{\mathrm{err}}}{kb} = \frac{(c\Delta T + \Delta b)}{b} = \frac{dl}{b}. \tag{7}$$

For an interferometer to function, this length error has to be much smaller than the wavelength $dl \ll \lambda = 2\pi/k$. We suppose that, at 10 MHz, NOIRE will at least fulfill $dl < \lambda/10$. This is verified with $\Delta b = 1$ m and $\Delta T = 3$ ns. Recent studies suggest that such accuracies could be achieved for NOIRE (Rajan & van der Veen, 2015; McPhee et al., 2024; Bernabeu et al., 2024).

With these accuracies, for a baseline of 100 km, the pointing error caused by the instrumental parameter is about 0.1 arminute. This error is comparable to the best accuracy levels observed in Figure 4 of the main article.

5 Simulation pipeline details

5.1 Signal modeling

The *RST* algorithm is meant to work at very low frequency, below 1 MHz. However, as mentioned previously, the sky remains mostly unknown in this spectral range. Novaco and Brown derived rough contour maps of the Galaxy using data from RAE 2 (Novaco & Brown, 1978) down to 1.31 MHz. These data enable to constrain the average brightness of the models but cannot be used to generate a source catalog. On the other hand, measurements performed with SunRISE (Kasper et al., 2021) could be used to confirm the detection level of a few bright sources. The commissioning phase of NOIRE will include a rough mapping of the sky, enabling the calibration of the source catalog to be used for the *RST* function. For the sake of the simulation, the low-frequency sky is approximated with a model derived from observations at higher frequency.

The measurements used by this algorithm are the correlation products measured between each pair of nodes, namely the interferometric visibilities. They are computed based on a sky model and a noise model. Since the interferometric visibilities are linear with the brightness from all directions, the contribution from each source can be computed independently. The noise is supposed to be uncorrelated so that it can be computed independently too. Its contribution to the visibilities is ξ. The sky model implemented is separated into two categories: diffuse emission and point sources whose contribution to the visibilities are respectively denoted by $\mathcal{V}_d$ and $\mathcal{V}_{\mathrm{ps}}$.

The total visibilities $\mathcal{V}$ can be expressed as $\mathcal{V} = \mathcal{V}_{ps} + \mathcal{V}_d + \xi$. The following subsections describe the first two contributions, whereas the noise model is discussed in the main article.

The sky model implemented does not take into account foreground sources and transient emissions, like, for instance, the solar radio bursts, the Earth Auroral Kilometric Radiation (AKR), or other planetary emissions.

5.1.1 Point source model

The point sources considered in this simulation are the point sources listed in the LOFAR database[1] at 60 MHz. More than 200 sources are taken from this database. The brightness of these sources are extrapolated to lower frequencies following the procedure described in Section 5.1.2.

For an unresolved source of brightness B_s and direction $\vec{s}$ its contribution to the visibilities is computed as (Carozzi, 2015; Thompson et al., 2017):

$$\mathcal{V}_s = B_s \exp\left(-ik\,\vec{b}\cdot\vec{s}\right) \tag{8}$$

The total contribution from all unresolved sources is $\mathcal{V}_{ps} = \sum_s \mathcal{V}_s$.

[1] `https://lcs165.lofar.eu/`

This modeling supposes that the sources not resolved by the instrument behave like point sources. However, low-frequency emissions are scattered when traversing the interstellar medium, enlarging their apparent angular sizes (Jester & Falcke, 2009). Depending on the frequency, their apparent angular size may be larger than the instrument's resolution.

5.1.2 Diffuse emission model

The contribution of the full sky diffuse emission is simulated using the Global Sky Model (GSM) map of the sky at 50 MHz (de Oliveira-Costa et al., 2008) as a reference. It is the lowest frequency map model that is almost complete. This map can be obtained in HEALPix format (Gorski et al., 2005) using the python interface `pyGDSM`[2] with an angular resolution scaling down to 7 arcmin, which is smaller than the angular resolution that can be achieved by NOIRE at 1 MHz.

As mentioned, the point sources are modeled separately from the continuum, whereas the GSM map already contains the signal coming from these sources. Plus, their signal is convolved with the impulse response of the instruments used for this survey. In order to adapt the model to our needs, the following steps are performed: for each point source selected in the catalog, a disc of radius $r_1 = 1.5°$ centered on the source position is uniformly set to a constant value. This value is the median brightness computed in the ring centered on the source and with inner and outer radii r_1 and 1.25 r_1. The radius is set to 1.5° in order to be larger than the widest point spread function (PSF) of the instrument used to generate this map.

Both the diffuse model and the point source model are extrapolated to lower frequencies. This extrapolation cannot be done using a simple power law as the low-frequency emissions are expected to be impacted by the electron free-free absorption (Jester & Falcke, 2009), as observed for the Galaxy around 2 MHz.

We chose to extrapolate the brightness of these sources below 2 MHz, by assuming that they share the same brightness spectrum with the Galaxy. The Galactic spectrum was modeled by Dulk, G. A. et al. (2001) using two power laws with a turnover at 2 MHz. With this approximation, the brightness temperature of the sources for $\nu < 2$ MHz, can be estimated with:

$$T(\nu) = T(60\text{MHz}) \left(\frac{60\text{MHz}}{2\text{MHz}}\right)^{-2.53} \left(\frac{\nu}{2\text{MHz}}\right)^{-0.3} \tag{9}$$

It would be more realistic to use different models for sources close to, or far from, the Galactic plane or to have a different treatment for extra-galactic sources. Still, the radio sky below 2 MHz remains mostly unknown, and no model available is close to reality. As such, we do not expect the RST's performance to be significantly more realistic with another model.

The computation of the contribution of the full sky diffuse emission is performed using the Spherical Wave Harmonic Transform (SWHT) method developed by Carozzi (2015).

[2] `https://github.com/telegraphic/pygdsm`

This method takes advantage of the compressed representation of the sky brightness distribution using spherical harmonics.

5.2 Evaluation of the accuracy

The output of the *RST* is a transform that includes a rotation. Its purpose is to provide directional information. The accuracy is evaluated as the maximum angular error that can be made. This is evaluated by comparing a vector $\vec{s}$ transformed by the simulated transform $\boldsymbol{\mathcal{M}}_{\text{simu}}$ and by the measured transform $\boldsymbol{\mathcal{M}}_{\text{meas}}$ returned by the *RST*. The directional error ϵ is expressed as:

$$\epsilon = \max_{\vec{s}} \quad \arccos\left((\boldsymbol{\mathcal{M}}_{\text{mes}} \cdot \vec{s}) \cdot (\boldsymbol{\mathcal{M}}_{\text{simu}} \cdot \vec{s})\right) \tag{10}$$

We compute this error for a direction $\hat{\vec{s}}$ that maximizes the error. Following Huynh (2009), we define $\hat{\vec{s}}$ as the cross product of $\vec{e}_x = (1, 0, 0)$ with $\vec{m}$, the rotation axis of ${\boldsymbol{\mathcal{M}}_{\text{mes}}}^T \boldsymbol{\mathcal{M}}_{\text{simu}}$. So that, $\hat{\vec{s}} = \vec{m} \wedge \vec{e}_x / \|\vec{m} \wedge \vec{e}_x\|$.

References

Bernabeu J. M., Ortega L., Blais A., GrÃ©goire Y., Chaumette E., 2024, On time-delay estimation accuracy limit under phase uncertainty, *in 2024 27th International Conference on Information Fusion (FUSION)*, pp 1–6, doi:10.23919/FUSION59988.2024.10706341

Carozzi T. D., 2015, Imaging on a sphere with interferometers: the spherical wave harmonic transform, *Monthly Notices of the Royal Astronomical Society: Letters*, *451, L6*

Dulk, G. A. Erickson, W. C. Manning, R. Bougeret, J.-L. 2001, Calibration of low-frequency radio telescopes using the galactic background radiation, *A&A*, *365, 294*

Gorski K. M., Hivon E., Banday A. J., Wandelt B. D., Hansen F. K., Reinecke M., Bartelmann M., 2005, HEALPix: A framework for high-resolution discretization and fast analysis of data distributed on the sphere, *The Astrophysical Journal*, *622, 759*

Huynh D. Q., 2009, Metrics for 3d rotations: Comparison and analysis, *Journal of Mathematical Imaging and Vision*, *35, 155*

Jester S., Falcke H., 2009, Science with a lunar low-frequency array: From the dark ages of the universe to nearby exoplanets, *New Astronomy Reviews*, *53, 1*

Kasper J., Lazio J., Romero-Wolf A., Lux J., Neilsen T., 2021, The sun radio interferometer space experiment (sunrise) mission, *in 2021 IEEE Aerospace Conference (50100)*, pp 1–11, doi:10.1109/AERO50100.2021.9438184

McPhee H., Tourneret J.-Y., Valat D., Delporte J., Grégoire Y., Paimblanc P., 2024, A robust time scale for space applications using the student's t-distribution, *Metrologia*, *61, 055010*

Novaco J. C., Brown L. W., 1978, Nonthermal galactic emission below 10 megahertz., *Astrophysical Journal*, *221, 114*

Rajan R. T., van der Veen A.-J., 2015, Joint Ranging and Synchronization for an Anchorless Network of Mobile Nodes, *IEEE Transactions on Signal Processing*, *63, 1925*

Thompson A. R., Moran J. M., Swenson G. W., 2017, Interferometry and synthesis in radio astronomy. Springer Nature

de Oliveira-Costa A., Tegmark M., Gaensler B., Jonas J., Landecker T., Reich P., 2008, A model of diffuse galactic radio emission from 10 mhz to 100 ghz, *Monthly Notices of the Royal Astronomical Society*, *388, 247*